Supplement of The Cryosphere, 19, 769–792, 2025
https://doi.org/10.5194/tc-19-769-2025-supplement

The Cryosphere
Open Access

Supplement of

Improving large-scale snow albedo modeling using a climatology of light-absorbing particle deposition

Manon Gaillard et al.

Correspondence to: Vincent Vionnet (vincent.vionnet@ec.gc.ca)

S1 Climatological data

S1.1 Snapshots

Figure S1 shows an example of median BC deposition from the GDFL database for a given date while an example of the GMASI snow cover product is presented on Fig. S2.

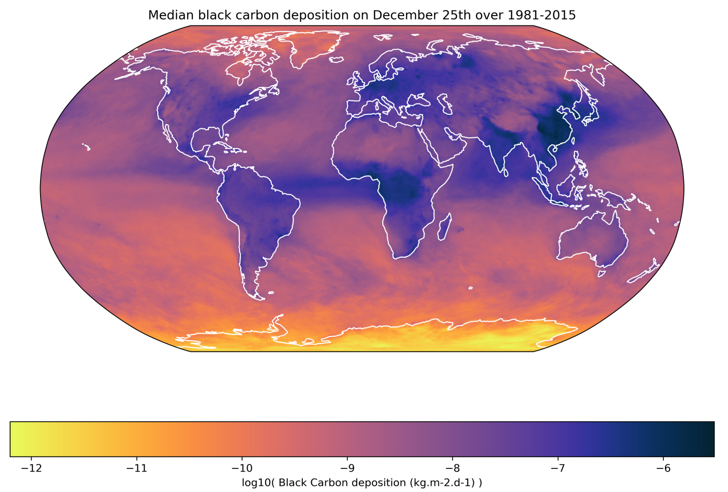

Figure S1. Map showing median BC deposition at the surface worldwide on December 25th from the GDFL database.

S1.2 Accuracy of the LAP climatology

Figure S3a shows the mean annual deposition flux in the Geophysical Fluid Dynamics Laboratory (GFDL) Coupled Model version 4 (Zhao et al., 2018) over the period 1981-2015 with Fig. S3b showing a zoom over the Tibetan Plateau. Observed mean annual dust deposition have been compiled at 26 sites around the world covering a large variety of aerosol load and elevation (Table S1). These data have been extracted from several studies listed in Table S1. The climatological mean annual dust deposition rates have then been extracted from the GFDL climatology at the location of these 26 sites. No correction of elevation difference between the GFDL model and the actual elevation of the site has been applied. Table S1 gives the mean annual dust deposition in the observation and the GFDL climatology at each site and Fig. S3c compares the two set of values. The GFDL climatology captures well the spatial variability of dust deposition around the globe. For example, it reproduces well the contrasted dust deposition patterns in Central Asia (Fig. Fig. S3b), where the maximum of dust deposition is found in the observation and in the GFDL dataset (site 1, Taklimakan). The lowest dust deposition rate in the observation and in the GFDL dataset are found in the Pacific ocean (sites 23 and 26), in central Greenland (site 25) and in the Antarctic Peninsula (site 24). At these two last sites, the GFDL dataset tends to overestimate the dust mean annual deposition rate by one order of magnitude.

The evaluation of the Black Carbon (BC) climatological deposition rates from the GFDL dataset is limited to three sites (Table S2). The same extraction methodology has been applied as for the dust climatological deposition rates. Table S2 shows that the LAP dataset captures the large differences in BC deposition between the Himalayan mountains (sites 1 and 2) and West Antarctica (site 3).

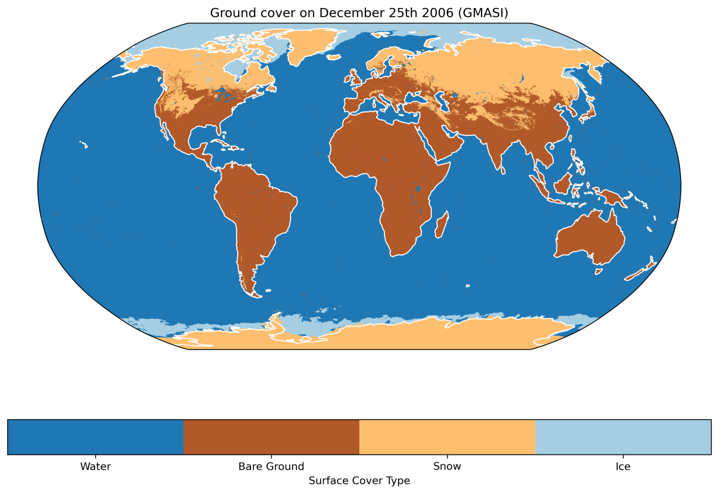

Figure S2. Map showing global surface covers taken from the GMASI product on December 25th, 2006.

S1.3 Inter-annual variability of LAP deposition on snow

Figure S4 shows the inter-annual range of the mean daily deposition rates over snow between a high and a low LAP year for BC, dust, and total LAP. This figure shows that this range (D_{high}-D_{low}) is typically on the same order of magnitude as the mean daily climatological deposition rates on snow (Fig. 7 in the main manuscript). The calculation of D_{high} and D_{low} is described in the main manuscript.

S2 Albedo observations and simulations

S2.1 Sodankylä forcing data

The meteorological forcing files for the Sodankylä site were built following the same methodology as Essery et al. (2016). To create these files, weather and radiation observations from the AWS at the Sodankylä research station (Finn. Met. Inst., 2018) were used. Hourly observations of surface pressure, precipitation, relative humidity and air temperature at 2 m, wind direction and speed at 10 m, and downward shortwave and longwave radiation were extracted over the 2007-2022 time period.

Gaps in these observations were filled using data from other sites in Northern Finland (Kittilä Kenttärova and Kittilä Lompolonvuoma, Finn. Met. Inst. (2021)). The remaining gaps after this were filled with ERA5 reanalysis data (Hersbach et al., 2020). The shortwave radiation was partitioned into direct and scattered radiation using the atmospheric model SB-DART (Ricchiazzi et al., 1998). As radiations are measured above canopy, the correction functions proposed by Essery et al. (2016) were applied to estimate radiative fluxes at the snow surface accounting for the impact of the surrounding trees.

S2.2 Snow depth threshold value for albedo evaluation

To limit the effect of ground contamination on the measurement of snow albedo, a threshold on snow depth has been applied to remove periods when the snow cover was not thick enough. A threshold value of 20 cm was selected for the sites below 60°N and 10 cm was used for the sites above 60°N (see main article). Snow albedo calculations using the online version of the snow

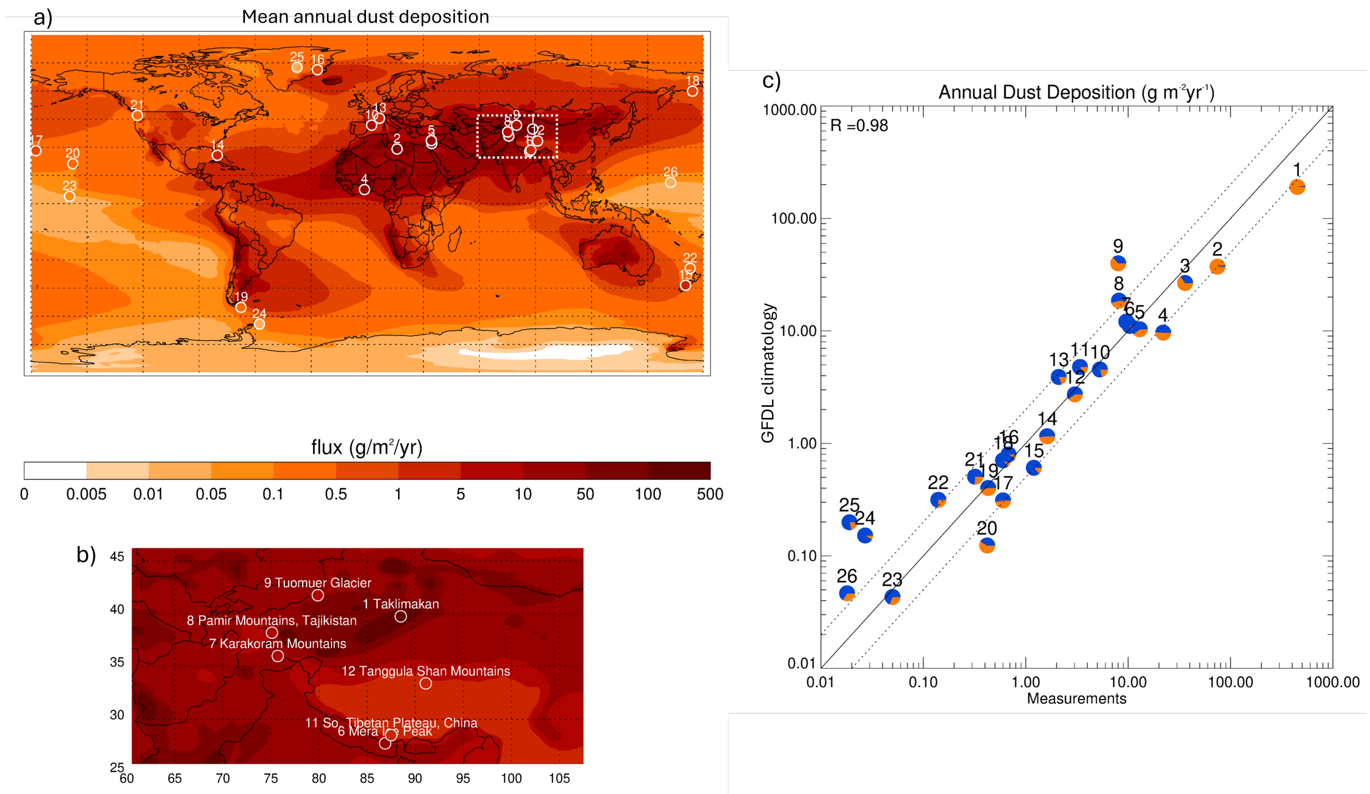

Figure S3. (a) Map showing the mean annual dust deposition from the GFDL climatology (1981-2015), (b) same as (a) for a region centered around the Tibetan Plateau and (c) scatter plot comparing the mean observed and simulated annual dust deposition at 26 sites around the globe. The location of these sites is shown on maps (a) and (b). For each site, the pie chart shows the decomposition in the GFDL climatology between dry (orange) and wet (blue) deposition. Detailed information about each site is provided in Table S1.

radiative transfer model SNICAR v3 Flanner et al. (2021) (http://snow.engin.umich.edu/) have been used to quantify the impact of ground contamination on broadband snow albedo for snow depth values corresponding to the threshold values selected in our study. Two snowpack have been considered: (i) a snowpack made of fresh snow with high SSA and low density values (typical of the accumulation season) and (ii) a snowpack made of melt forms) with low SSA and high density values (typical of the ablation season. The SSA and density values for each type of snow were taken from Domine et al. (2007). A ground albedo of 0.25, typical of grass, was selected and the default options for SNICAR were used. The results are presented in Table S3 below. For a 10-cm (20-cm) thick snowpack made of fresh snow, the ground contamination reduces the snow albedo by 0.8 % (0.2 %). For a 10-cm (20-cm) thick snowpack made of melt forms, the ground contamination reduces the snow albedo by 1.9 % (0.6 %). These results confirm that the threshold values on snow depth applied in this study are sufficient to limit the impact of ground contamination on the snow albedo measurements, allowing a robust comparison between simulated and observed snow albedo.

S2.3 Numbers of days for the evaluation

A minimal snow age for the surface snow layer, A_{lim}, is considered to select evaluation periods when the impact of LAPs on snow albedo was significant. Table S4 shows the average number of days selected per year for the evaluation of snow albedo simulations at each of the sites considered in this study.

Table S1. Mean annual dust deposition in the observations and in the GFDL climatology at 26 sites. The numbers correspond to the number shown on Fig. S3.

Num.	Name	Lat. (^{o}N)	Lon. (^{o}E)	Elev. (m)	Reference	Obs. (g $m^{-2}yr^{-1}$)	Clim. (g $m^{-2}yr^{-1}$)
1	Taklimakan	39.75	88.50	200.	Zhang et al. (1998)	450.00	177.37
2	Waddan	29.12	15.93	2.	O'Hara et al. (2006)	74.53	34.61
3	Tel Aviv	32.00	34.50	40.	Ganor and Mamane (1982)	36.00	26.87
4	Ghana, Gulf of Guinea	7.50	-1.50	0.	Resch et al. (2008)	22.00	9.66
5	Erdemli	33.57	34.26	21.	Kubilay et al. (2000)	13.00	9.99
6	Mera Ice Peak	27.72	86.87	6376.	Ginot et al. (2014)	10.40	11.39
7	Karakoram Mtns	36.00	75.70	5150.	Wake et al. (1994)	9.60	11.28
8	Pamir Mtns	38.20	75.10	5910.	Wake et al. (1994)	8.14	20.27
9	Tuomuer Glacier	41.75	79.87	4600.	Zhiwen and Zhongqin (2011)	8.00	31.69
10	Montseny Mtns	41.80	2.30	700.	Avila et al. (1997)	5.30	4.64
11	So. Tibetan Plateau	28.50	87.50	5850./6140.	Wake et al. (1994)	3.39	5.28
12	Tanggula Shan Mtns	33.40	91.10	5950.	Wake et al. (1994)	3.02	2.81
13	French Alps	45.50	6.50	4270.	De Angelis and Gaudichet (1991)	2.10	3.81
14	Miami	25.75	-80.25	10.	Prospero et al. (1987)	1.62	1.10
15	Tasman Glacier	-43.50	170.30	2600.	Windom (1969)	1.20	0.82
16	Renland	71.30	-26.70	2340.	Bory et al. (2003)	0.68	0.73
17	Midway	28.20	-177.35	4.	Prospero (1989)	0.60	0.28
18	Shemya	59.92	174.00	2.	Prospero (1989)	0.60	0.65
19	Navarino Island	-55.22	-67.62	35.	Sapkota et al. (2007)	0.43	0.53
20	Oahu	21.30	-157.60	20.	Prospero (1989)	0.42	0.13
21	Mount Olympus	47.00	-123.00	2000.	Windom (1969)	0.32	0.47
22	New Zealand	-34.50	172.75	2.	Arimoto et al. (1990)	0.14	0.41
23	Fanning	3.90	-159.30	25.	Prospero (1989)	0.05	0.04
24	James Ross Island	-64.20	-57.70	1542.	McConnell et al. (2007)	0.03	0.20
25	GRIP	72.60	-37.60	3232.	Bory et al. (2003)	0.02	0.18
26	Enewetak	11.30	162.30	5.	Arimoto et al. (1985)	0.02	0.04

Table S2. Mean annual black carbon deposition in the observations and in the GFDL climatology at three sites.

Num.	Name	Lat. (^{o}N)	Lon. (^{o}E)	Elev. (m)	Reference	Obs. (g $m^{-2}yr^{-1}$)	Clim. (g $m^{-2}yr^{-1}$)
1	Nepal Clim. Obs.- Pyramid	27.95	86.80	5079.	Yasunari et al. (2010)	112.00	179.83
2	Tibet Palong-Zanbu Glacier	29.21	96.92	5500.	Xu et al. (2009)	29.40	77.40
3	West Antarctic Ice Sheet	-79.46	-112.08	1766.	Bisiaux et al. (2012)	0.02	0.07

S2.4 Performances of albedo simulations

Errors metrics (bias and RMSE) for each site are shown as boxplot for different values of γ on Fig. S5 to Fig. S13.

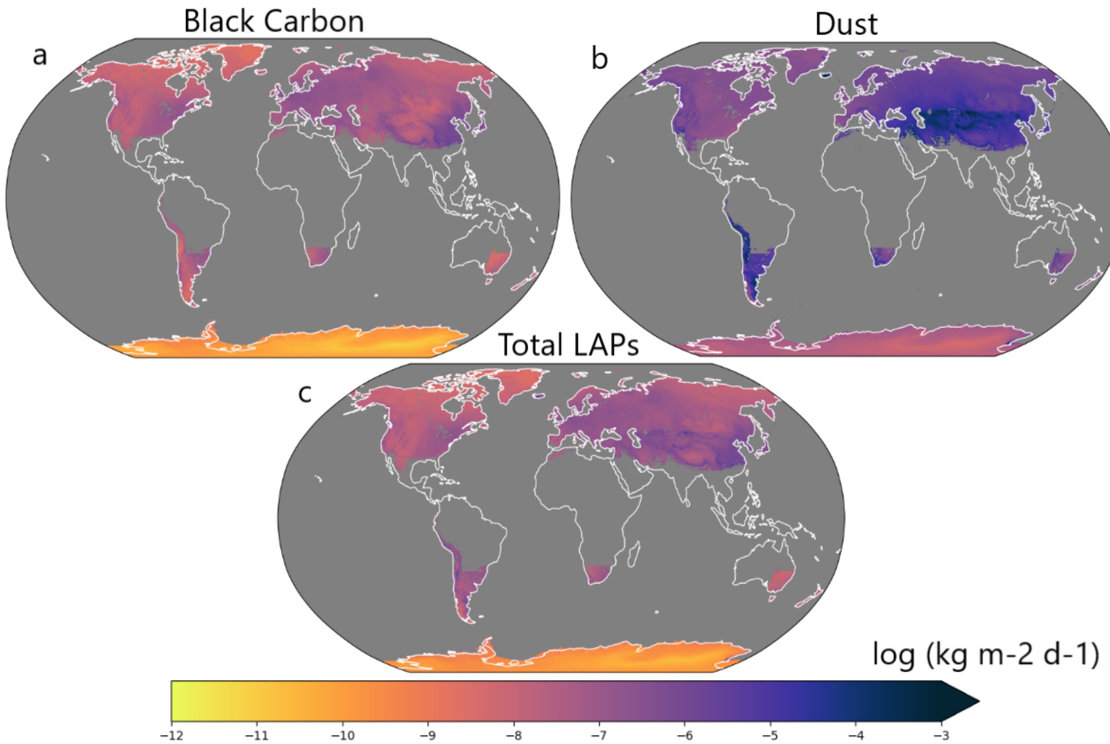

Figure S4. Global maps of the inter-annual range of the daily-average (a) BC, (b) dust, and (c) total LAP (BC + dust in equivalent BC) deposition rates over snow between a high and a low LAP year (D_{high}-D_{low}).

Table S3. Snow albedo computed by SNICAR v3 for 2 different snowpack of various depth.

	Snow albedo values for different snow depth		
Type of snowpack and ground	Depth=0.1 m	Depth=0.2 m	Depth=100 m
SSA= 65 m^2 kg^{-1} Density= 150 kg m^{-3} Ground albedo = 0.25 No LAP	0.841090	0.846047	0.848279
SSA= 10 m^2 kg^{-1} Density= 300 kg m^{-3} Ground albedo = 0.25 No LAP	0.772633	0.782954	0.787879

Table S4. Average number of days selected per year for the evaluation of snow albedo simulations at each of the sites considered in this study

Site	Days selected
Bylot	39
Col de Porte	42
Kühtai	47
Sapporo	12
Senator Beck	45
Sodankylä	30
Swamp Angel	41
Trail Valley Creek	42
Umiujaq	40
Weissfluhjoch	73

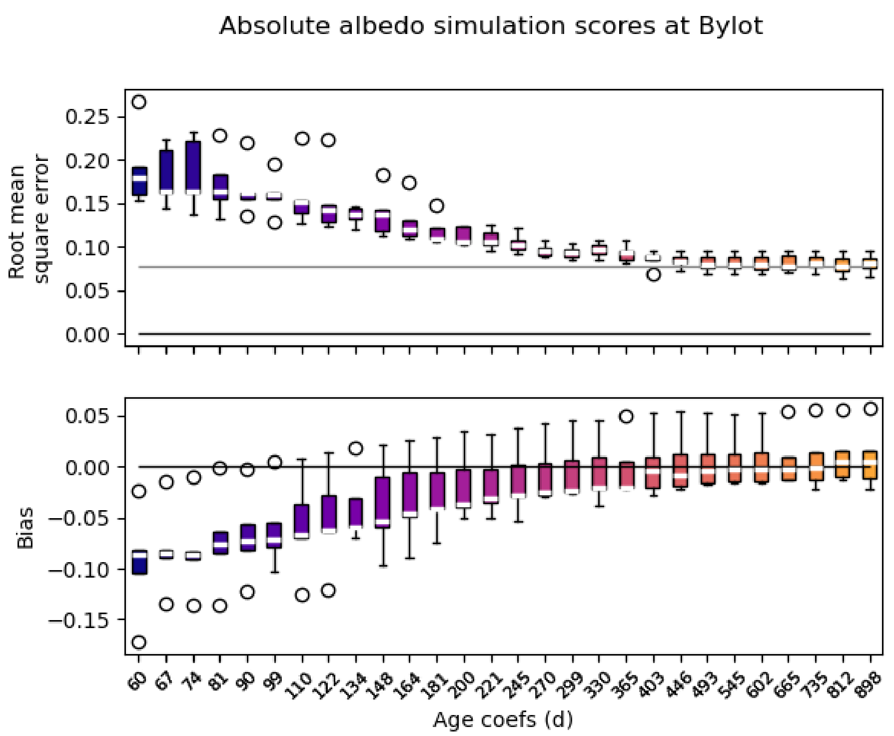

Figure S5. Box plot showing the scores at the Bylot site, in the second round of scoring. The median over the years for each γ is shown in white. The box plots show the interquartile values, and outliers are plotted as circles.

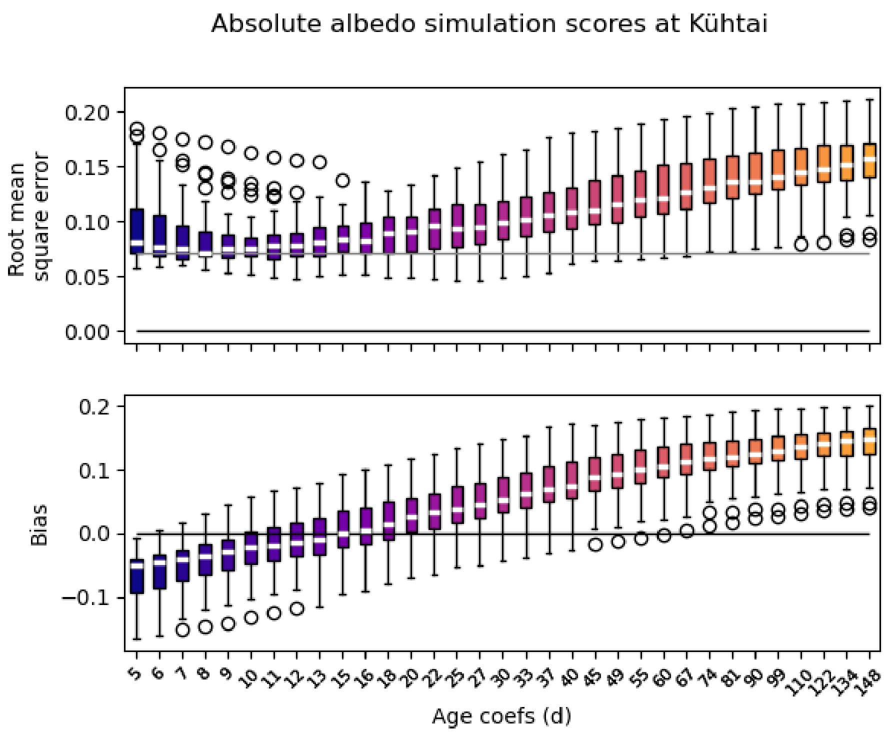

Figure S6. Box plot showing the scores at the Kühtai site, in the second round of scoring. The median over the years for each γ is shown in white. The box plots show the interquartile values, and outliers are plotted as circles.

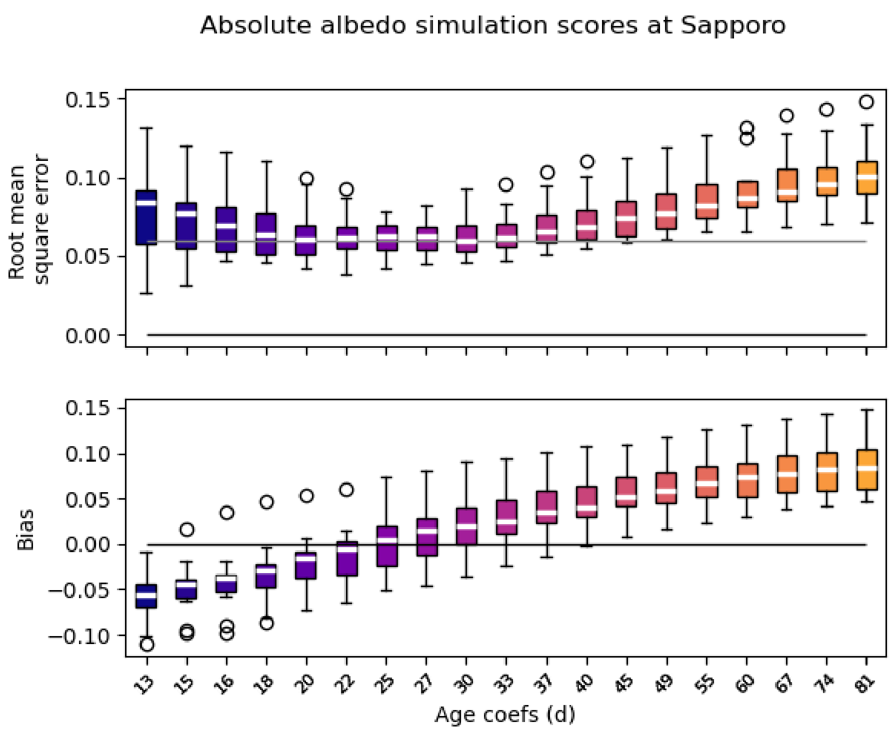

Figure S7. Box plot showing the scores at the Sapporo site, in the second round of scoring. The median over the years for each γ is shown in white. The box plots show the interquartile values, and outliers are plotted as circles.

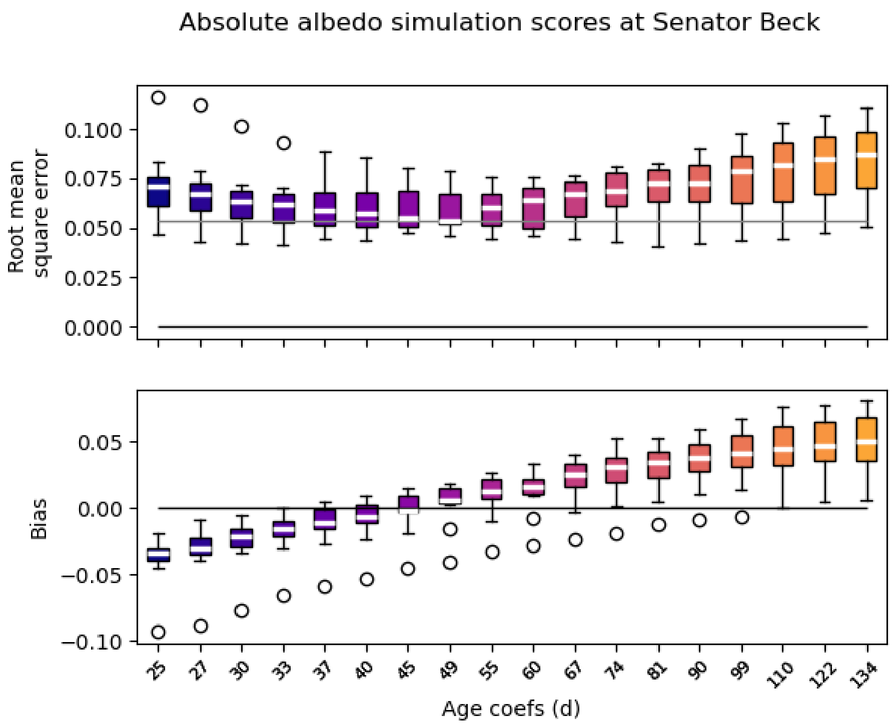

Figure S8. Box plot showing the scores at the Senator Beck site, in the second round of scoring. The median over the years for each γ is shown in white. The box plots show the interquartile values, and outliers are plotted as circles.

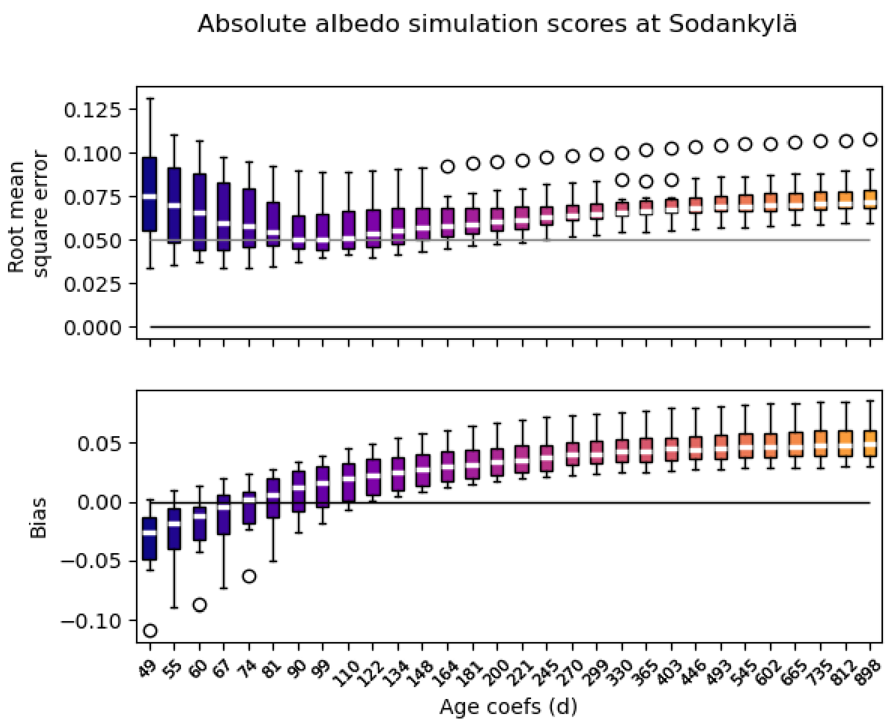

Figure S9. Box plot showing the scores at the Sodankylä site, in the second round of scoring. The median over the years for each γ is shown in white. The box plots show the interquartile values, and outliers are plotted as circles.

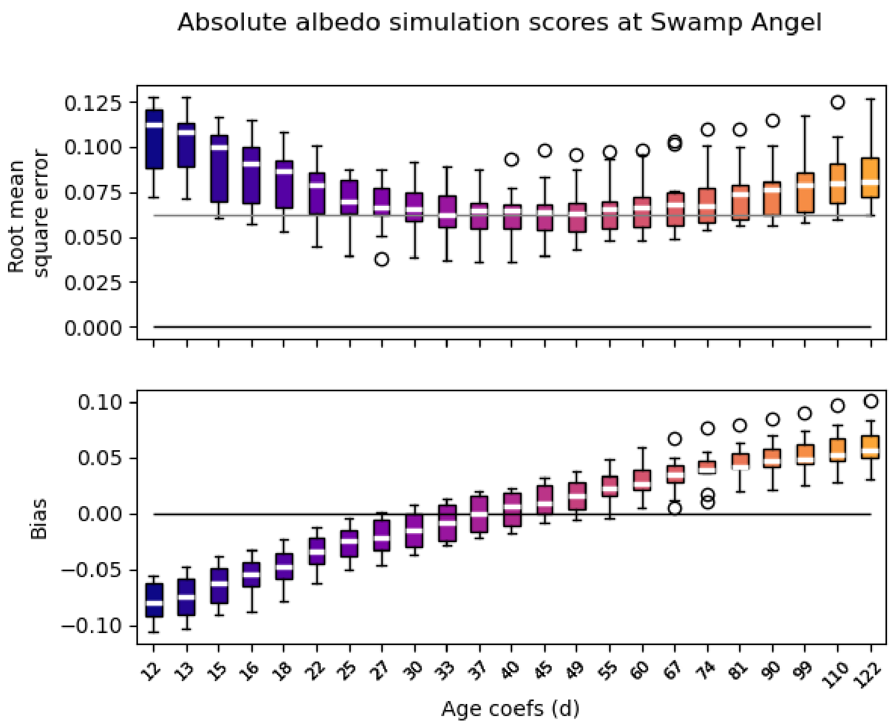

Figure S10. Box plot showing the scores at the Swamp Angel site, in the second round of scoring. The median over the years for each γ is shown in white. The box plots show the interquartile values, and outliers are plotted as circles.

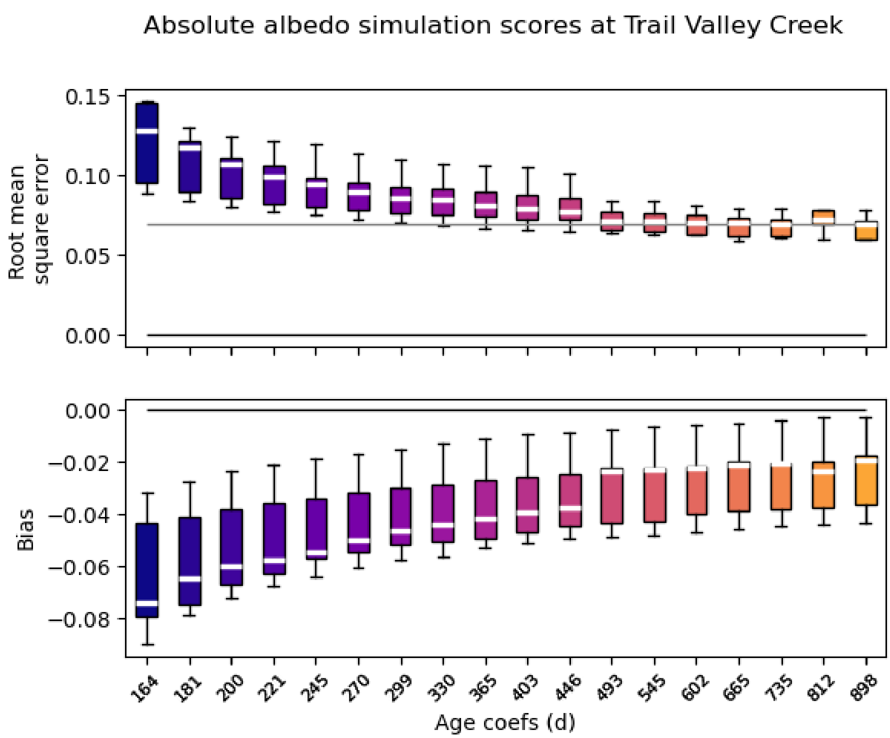

Figure S11. Box plot showing the scores at the Trail Valley Creek site, in the second round of scoring. The median over the years for each γ is shown in white. The box plots show the interquartile values, and outliers are plotted as circles.

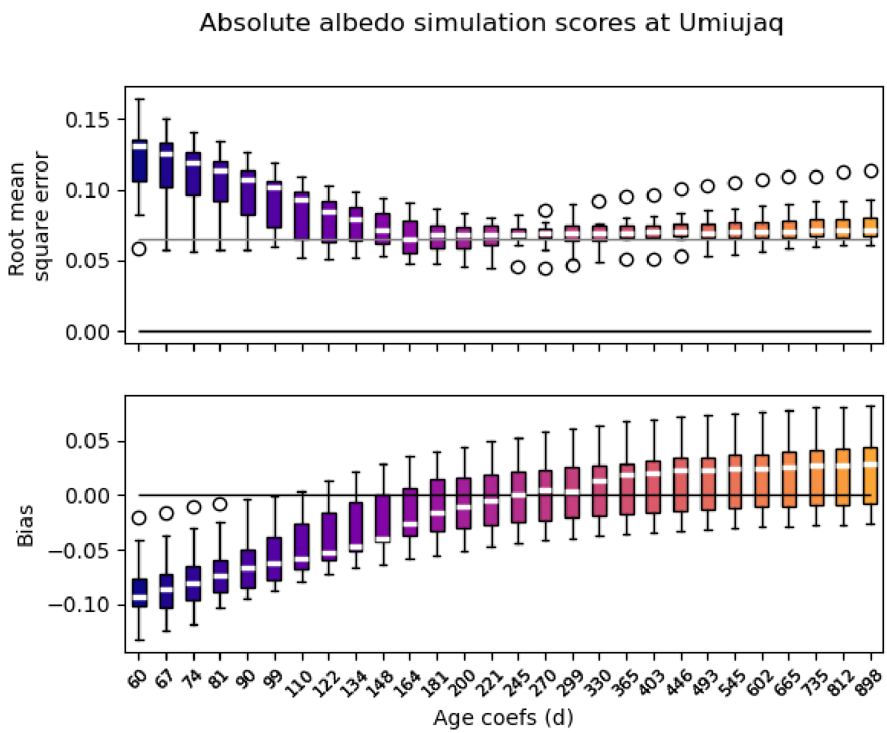

Figure S12. Box plot showing the scores at the Umiujaq site, in the second round of scoring. The median over the years for each γ is shown in white. The box plots show the interquartile values, and outliers are plotted as circles.

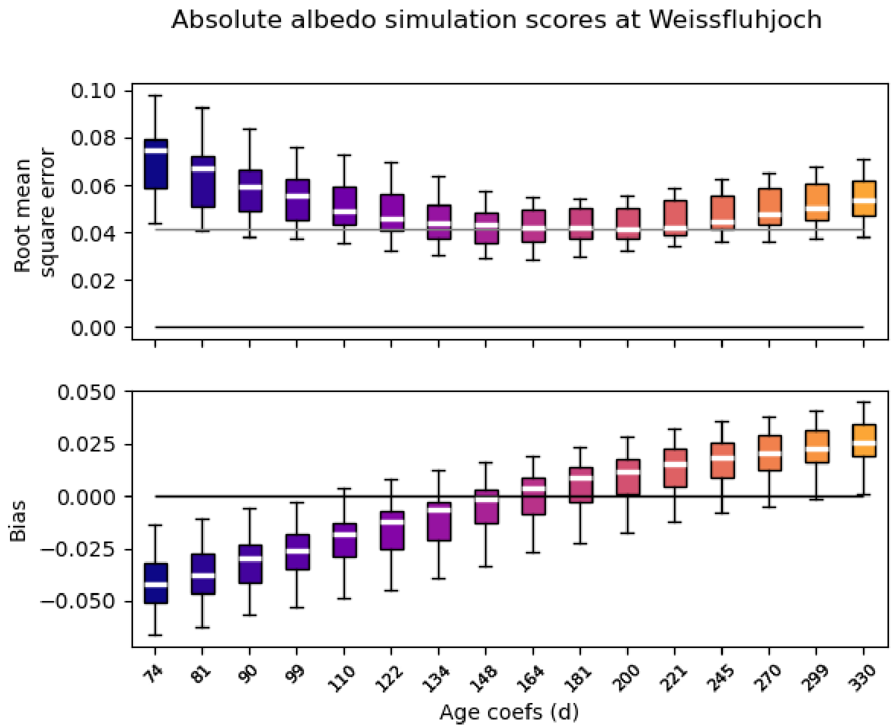

Figure S13. Box plot showing the scores at the Weissfluhjoch site, in the second round of scoring. The median over the years for each γ is shown in white. The box plots show the interquartile values, and outliers are plotted as circles.

References

Arimoto, R., Duce, R., Ray, B., and Unni, C.: Atmospheric trace elements at Enewetak Atoll: 2. Transport to the ocean by wet and dry deposition, Journal of Geophysical Research: Atmospheres, 90, 2391–2408, 1985.

Arimoto, R., Ray, B. J., Duce, R. A., Hewitt, A. D., Boldi, R., and Hudson, A.: Concentrations, sources, and fluxes of trace elements in the remote marine atmosphere of New Zealand, Journal of Geophysical Research: Atmospheres, 95, 22 389–22 405, 1990.

Avila, A., Queralt-Mitjans, I., and Alarcón, M.: Mineralogical composition of African dust delivered by red rains over northeastern Spain, Journal of Geophysical Research: Atmospheres, 102, 21 977–21 996, 1997.

Bisiaux, M., Edwards, R., McConnell, J., Albert, M., Anschütz, H., Neumann, T., Isaksson, E., and Penner, J.: Variability of black carbon deposition to the East Antarctic Plateau, 1800–2000 AD, Atmospheric Chemistry and Physics, 12, 3799–3808, 2012.

Bory, A.-M., Biscaye, P., Piotrowski, A., and Steffensen, J.: Regional variability of ice core dust composition and provenance in Greenland, Geochemistry, Geophysics, Geosystems, 4, 2003.

De Angelis, M. and Gaudichet, A.: Saharan dust deposition over Mont Blanc (French Alps) during the last 30 years, Tellus B, 43, 61–75, 1991.

Domine, F., Taillandier, A.-S., and Simpson, W. R.: A parameterization of the specific surface area of seasonal snow for field use and for models of snowpack evolution, 112, 2007.

Essery, R., Kontu, A., Lemmetyinen, J., Dumont, M., and Ménard, C. B.: A 7-year dataset for driving and evaluating snow models at an Arctic site (Sodankylä, Finland), Geoscientific Instrumentation, Methods and Data Systems, 5, 219–227, 2016.

Finn. Met. Inst.: Finnish Meteorological Institute - Radiation and snow depth data at Sodankylä Peatland Site, https://litdb.fmi.fi/peatland.php, observations from the Arctic Space Centre, 2018.

Flanner, M. G., Arnheim, J. B., Cook, J. M., Dang, C., He, C., Huang, X., Singh, D., Skiles, S. M., Whicker, C. A., and Zender, C. S.: SNICAR-ADv3: a community tool for modeling spectral snow albedo, Geoscientific Model Development, 14, 7673–7704, 2021.

Ganor, E. and Mamane, Y.: Transport of Saharan dust across the eastern Mediterranean, Atmospheric Environment (1967), 16, 581–587, 1982.

Ginot, P., Dumont, M., Lim, S., Patris, N., Taupin, J.-D., Wagnon, P., Gilbert, A., Arnaud, Y., Marinoni, A., Bonasoni, P., et al.: A 10 year record of black carbon and dust from a Mera Peak ice core (Nepal): variability and potential impact on melting of Himalayan glaciers, The Cryosphere, 8, 1479–1496, 2014.

Hersbach, H., Bell, B., Berrisford, P., Hirahara, S., Horányi, A., Muñoz-Sabater, J., Nicolas, J., Peubey, C., Radu, R., Schepers, D., et al.: The ERA5 global reanalysis, Quarterly Journal of the Royal Meteorological Society, 146, 1999–2049, 2020.

Kubilay, N., Nickovic, S., Moulin, C., and Dulac, F.: An illustration of the transport and deposition of mineral dust onto the eastern Mediterranean, Atmospheric Environment, 34, 1293–1303, 2000.

McConnell, J. R., Aristarain, A. J., Banta, J. R., Edwards, P. R., and Simões, J. C.: 20th-Century doubling in dust archived in an Antarctic Peninsula ice core parallels climate change and desertification in South America, Proceedings of the National Academy of Sciences, 104, 5743–5748, 2007.

O'Hara, S. L., Clarke, M. L., and Elatrash, M. S.: Field measurements of desert dust deposition in Libya, Atmospheric Environment, 40, 3881–3897, 2006.

Prospero, J. M.: Mineral aerosol transport to the Pacific Ocean, Chemical oceanography, 10, 188–218, 1989.

Prospero, J. M., Nees, R. T., and Uematsu, M.: Deposition rate of particulate and dissolved aluminum derived from Saharan dust in precipitation at Miami, Florida, Journal of Geophysical Research: Atmospheres, 92, 14 723–14 731, 1987.

Resch, F., Sunnu, A., and Afeti, G.: Saharan dust flux and deposition rate near the Gulf of Guinea, Tellus B: Chemical and Physical Meteorology, 60, 98–105, 2008.

Ricchiazzi, P., Yang, S., Gautier, C., and Sowle, P.: Sbdart : A research and teaching software tool for plane-parallel radiative transfer in the earth's atmosphere, Bulletin of the American Meteorological Society, 10, 2101–2114, https://doi.org/10.1175/1520-0477(1998)079<2101:SARATS>2.0.CO;2, 1998.

Sapkota, A., Cheburkin, A. K., Bonani, G., and Shotyk, W.: Six millennia of atmospheric dust deposition in southern South America (Isla Navarino, Chile), The Holocene, 17, 561–572, 2007.

Wake, C. P., Mayewski, P. A., Li, Z., Han, J., and Qin, D.: Modern eolian dust deposition in central Asia, Tellus B: Chemical and Physical Meteorology, 46, 220–233, 1994.

Windom, H. L.: Atmospheric dust records in permanent snowfields: Implications to marine sedimentation, Geological Society of America Bulletin, 80, 761–782, 1969.

Xu, B.-Q., Wang, M., Joswiak, D. R., Cao, J.-J., Yao, T.-D., Wu, G.-J., Yang, W., and Zhao, H.-B.: Deposition of anthropogenic aerosols in a southeastern Tibetan glacier, Journal of Geophysical Research: Atmospheres, 114, 2009.

Yasunari, T., Bonasoni, P., Laj, P., Fujita, K., Vuillermoz, E., Marinoni, A., Cristofanelli, P., Duchi, R., Tartari, G., and Lau, K.-M.: Estimated impact of black carbon deposition during pre-monsoon season from Nepal Climate Observatory–Pyramid data and snow albedo changes over Himalayan glaciers, Atmospheric Chemistry and Physics, 10, 6603–6615, 2010.

Zhang, X. Y., Arimoto, R., Zhu, G., Chen, T., and Zhang, G.: Concentration, size-distribution and deposition of mineral aerosol over Chinese desert regions, Tellus B: Chemical and Physical Meteorology, 50, 317–330, 1998.

Zhao, M., Golaz, J.-C., Held, I. M., Guo, H., Balaji, V., Benson, R., Chen, J.-H., Chen, X., Donner, L. J., Dunne, J. P., Dunne, K., Durachta, J., Fan, S.-M., Freidenreich, S. M., Garner, S. T., Ginoux, P., Harris, L. M., Horowitz, L. W., Krasting, J. P., Langenhorst, A. R., Liang, Z., Lin, P., Lin, S.-J., Malyshev, S. L., Mason, E., Milly, P. C. D., Ming, Y., Naik, V., Paulot, F., Paynter, D., Phillipps, P., Radhakrishnan, A., Ramaswamy, V., Robinson, T., Schwarzkopf, D., Seman, C. J., Shevliakova, E., Shen, Z., Shin, H., Silvers, L. G., Wilson, J. R., Winton, M., Wittenberg, A. T., Wyman, B., and Xiang, B.: The GFDL Global Atmosphere and Land Model AM4.0/LM4.0: 1. Simulation Characteristics With Prescribed SSTs, Journal of Advances in Modeling Earth Systems, 10, 691–734, https://doi.org/10.1002/2017MS001208, 2018.

Zhiwen, D. and Zhongqin, L.: Characteristics of atmospheric dust deposition in snow on glacier no. 72, Mount Tuomuer, China, Arctic, Antarctic, and Alpine Research, 43, 517–526, 2011.